01 Jan 2023

Enhancing Near-Field Wireless Localization with LiDAR-Assisted RIS in Multipath Environments

Omar Rinch

Ahmed Elzanaty

Ahmad Alsharoa
Missouri University of Science and Technology, aalsharoa@mst.edu

Recommended Citation

O. Rinch et al., "Enhancing Near-Field Wireless Localization with LiDAR-Assisted RIS in Multipath Environments," *IEEE Wireless Communications Letters*, Institute of Electrical and Electronics Engineers, Jan 2023.
The definitive version is available at https://doi.org/10.1109/LWC.2023.3311730

Enhancing Near-Field Wireless Localization with LiDAR-Assisted RIS in Multipath Environments

Omar Rinch, *Student Member, IEEE,* Ahmed Elzanaty, *Senior Member, IEEE,* Ahmad Alsharoa, *Senior Member, IEEE*

***Abstract*—In next-generation wireless networks that adopt millimeter-waves and large reconfigurable intelligent surfaces (RISs), the user is expected to be in the near-field region, where the widely adopted far-field algorithms based on far-field can yield low positioning accuracy. Also, the localization of user equipment (UE) becomes more challenging in multipath environments. In this paper, we propose a localization algorithm for a UE in the near-field of a RIS in multipath environments. The proposed scheme utilizes a light detection and ranging (LiDAR) to assist the UE positioning by providing geometric information about some of the scatterers in the environment. This information is fed to a sparse recovery algorithm to improve the localization accuracy of the UE by reducing the number of variables (i.e., angle of arrivals and distances) to be estimated. The numerical results show that the proposed scheme can improve the localization accuracy by 65% compared to the standard compressed sensing (CS) scheme.**

***Index Terms*—Reconfigurable intelligent surface (RIS); light detection and ranging (LiDAR); wireless localization; near-field.**

I. Introduction

With the increasing demand for centimeter-level localization accuracy, future networks are expected to enable accurate localization aided by sensing systems [1]. However, poor channels with non-line of sight (NLoS) component can limit the performance of such systems. In this regard, a reconfigurable intelligent surface (RIS) can be considered to create a non-direct line-of-sight (LoS) link that enhances positioning [2].

The advent of millimeter-wave (mm-wave) communications have introduced spatial sparsity in the channel model, providing a unique opportunity to apply sparse recovery localization techniques. For instance, works such as [3] and [4] exploit the sparsity in the channel model to propose an RIS-aided localization algorithm with high accuracy by considering a continuous domain for the sparse localization variables, i.e., atomic norm minimization. However, the utilization of mm-wave and large surfaces such as the RIS can promote near-field channel models where coupling between the bearing angles and the distances exist due to the considerable curvature of the wavefront of the received signals [5]. As a result, the method in [3] is constrained by the near-field computational optimization complexity and is not straightforward to be extended to multipath environments while the model in [4] considers far-field only. Such coupling can be relaxed by exploiting the spatial symmetry in the uniform linear array (ULA) structure along with an on-grid sparse recovery algorithm, promoting a less complex solution that can be applied in multipath environments [6]. However, the accuracy is still limited by the considered resolution for angles and distances, i.e., quantization errors in compressed sensing (CS).

The limited number of radio-frequency (RF) chains restricts the CS measurements, thereby affecting the capability to detect multipath components and consequently reducing localization accuracy. A viable strategy to address this is the integration of sensors, specifically light detection and ranging (LiDAR). By supplying geometric information, LiDAR can improve the detection of multipath components. LiDAR's utility extends beyond this; for example, [7] employed LiDAR for LoS blockage prediction, while [8] and [9] used LiDAR for predicting future BS beams from a codebook. Yet, its application in enhancing RIS-aided near-field wireless localization remains unexplored.

In this paper, we propose using LiDAR to enhance near-field RIS localization of user equipment (UE). We employ a base station (BS) with LiDAR sensors to estimate the location of scatterers within its field of view. These locations are input to a CS-based algorithm as partial support, and the CS is used to estimate the UE location. The contributions of this paper are as follows:

- We propose enhancing RIS-aided near-field wireless localization by utilizing LiDAR technology to gain insights into the multipath environment.
- We propose LiDAR data processing technique that takes the LiDAR three dimensional (3D) cloud data measurements as input and estimates the locations of the scatterers in the environment as an output.
- We modify the received measurements to decouple the range and bearing angles due to the near-field.
- We feed the location of the detected scatterers to CS algorithm as partial support to localize the UE.
- We further use the estimated scatterers' locations to optimize the RIS such that we maximize the signal-to-noise ratio (SNR) at the receiver.

Notation: Matrices are denoted by capital and bold letters $\mathbf{X}$, vectors are denoted by bold and lowercase letters $\mathbf{x}$, and scalars are denoted by non-bold letters x or X. The transpose, conjugate, pseudo-inverse, and Hermitian transpose operators are $(.)^T$, $(.)^*$, $(.)^\dagger$, and $(.)^H$, respectively. diag$(.)$ converts a vector into a diagonal matrix, $\mathbf{I}_{N^{\mathrm{U}}}$ is an identity matrix of size N^{U}, $||.||_{2,1}$ and $||.||_F$ are the L2 over L1 norm and the Frobenius norms. $\mathbf{x}_l$, $\mathbf{x}_{b*}$, and $x_{b,l}$ are the l^{th} column, b^{th} row, and b^{th} element of the l^{th} column of $\mathbf{X}$, respectively. $\mathcal{U} \triangleq \{-U, -U+1, \cdots, U\}$ and $\mathcal{B} \triangleq \{-B, -B+1, \cdots, B\}$.

II. System Model

We consider a wireless localization system that consists of a UE, BS, and RIS located at $\mathbf{p}^{\mathrm{U}} = [x^{\mathrm{U}}, y^{\mathrm{U}}]^T$, $\mathbf{p}^{\mathrm{B}} = [x^{\mathrm{B}}, y^{\mathrm{B}}]^T$,

O. Rinchi and A. Alsharoa are with the Electrical and Computer Engineering Department, Missouri University of Science and Technology, Rolla, USA. (E–mail: {omar.rinchi, aalsharoa}@mst.edu).

A. Elzanaty is with the 5GIC & 6GIC, Institute for Communication Systems (ICS), University of Surrey, Guildford, GU2 7XH, United Kingdom. (E–mails: a.elzanaty@surrey.ac.uk).

This article has been accepted for publication in IEEE Wireless Communications Letters. This is the author's version which has not been fully edited and content may change prior to final publication. Citation information: DOI 10.1109/LWC.2023.3311730

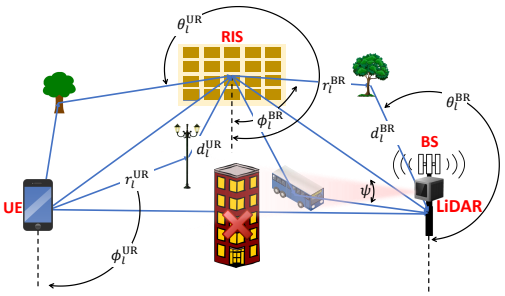

Fig. 1: The proposed system scenario and architecture.

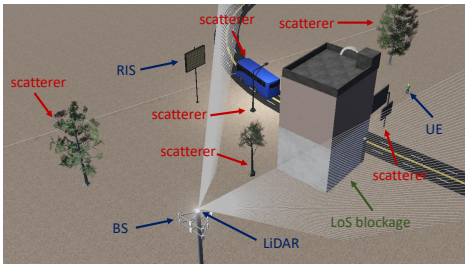

Fig. 2: Simulated scenario using Webots.

and $\mathbf{p}^{\mathrm{R}} = [x^{\mathrm{R}}, y^{\mathrm{R}}]^T$, respectively. We consider multiple-input multiple-output (MIMO) orthogonal frequency-division multiplexing (OFDM) system with flat fading characteristics where the number of antennas in the UE, BS, and the RIS are given as $N^{\mathrm{U}}, N^{\mathrm{B}}$, and N^{R}, respectively. We assume that all the stations are equipped with ULAs. We consider a multipath environment where multiple scatterers are involved with L^{BR} and L^{UR} being the number of scatterers/paths between the (BS and the RIS) and the (RIS and the UE) respectively. The l-th scatterers is located at $\mathbf{p}_l^{\mathrm{S,BR}} = [x_l^{\mathrm{BR}}, y_l^{\mathrm{BR}}]^T$ and $\mathbf{p}_l^{\mathrm{S,UR}} = [x_l^{\mathrm{UR}}, y_l^{\mathrm{UR}}]^T$. We assume that the LoS between the BS and the UE is blocked by an obstacle. The BS is also equipped with a LiDAR sensor located exactly at the BS location $\mathbf{p}^{\mathrm{B}}$ with a horizontal field of view angle ψ and number of layers N^{layers}. Our model considers an uplink positioning where the BS retrieves the location of the UE from its uplink signal arrived through the RIS.[1] Fig. 1 illustrates the system scenario. The received signal at the BS is expressed as

$$\mathbf{Y} = \mathbf{H}\,\mathbf{X} + \mathbf{Z}, \tag{1}$$

where $\mathbf{X} \in \mathbb{C}^{N^{\mathrm{U}} \times M^{\mathrm{o}}}$ represents the OFDM positioning reference signal (PRS) transmitted over M^{o} narrowband sub-channels that are orthogonal with with power P, i.e, $\mathbf{X}\mathbf{X}^{\mathrm{H}} = \frac{P}{N^{\mathrm{U}}}\mathbf{I}_{N^{\mathrm{U}}}$, and $\mathbf{Z} \in \mathbb{C}^{N^{\mathrm{B}} \times M^{\mathrm{o}}}$ represents the additive white Gaussian noise (AWGN) where $z_{i,j} \sim \mathcal{CN}(0, \sigma_z^2)$. The overall channel matrix between the UE and the BS can be modeled as a narrowband channel model as [10], [11]

$$\mathbf{H} = \mathbf{H}^{\mathrm{BR}} \mathrm{diag}(\boldsymbol{\Theta}) \mathbf{H}^{\mathrm{UR}}, \tag{2}$$

where $\mathrm{diag}(\boldsymbol{\Theta}) \in \mathbb{C}^{N^{\mathrm{R}} \times N^{\mathrm{R}}}$ is a matrix that represents the phase control of the RIS where $\boldsymbol{\Theta} \triangleq \left[\zeta_1 e^{j\theta_1}, \zeta_2 e^{j\theta_2}, \cdots, \zeta_{N^{\mathrm{R}}} e^{j\theta_{N^{\mathrm{R}}}}\right]^T$ and $\zeta_r = 1$ as we consider ideal RIS, and $\mathbf{H}^{\mathrm{BR}} \in \mathbb{C}^{N^{\mathrm{B}} \times N^{\mathrm{R}}}$ represents the channel between the RIS and the BS while $\mathbf{H}^{\mathrm{UR}} \in \mathbb{C}^{N^{\mathrm{R}} \times N^{\mathrm{U}}}$ is the channel between the UE and the RIS. We have

$$\mathbf{H}^{\mathrm{BR}} = \mathbf{A}(\boldsymbol{\theta}^{\mathrm{BR}}, \mathbf{d}^{\mathrm{BR}})\, \mathrm{diag}\left(\boldsymbol{\rho}^{\mathrm{BR}}\right)\, \mathbf{A}^H(\boldsymbol{\phi}^{\mathrm{BR}}, \mathbf{r}^{\mathrm{BR}}), \tag{3}$$

where $\mathbf{A}(\boldsymbol{\theta}^{\mathrm{BR}}, \mathbf{d}^{\mathrm{BR}}) \in \mathbb{C}^{N^{\mathrm{B}} \times L^{\mathrm{BR}}}$ and $\mathbf{A}(\boldsymbol{\phi}^{\mathrm{BR}}, \mathbf{r}^{\mathrm{BR}}) \in \mathbb{C}^{N^{\mathrm{R}} \times L^{\mathrm{BR}}}$ represents the steering matrices at the BS and the RIS, respectively. The angles $\boldsymbol{\phi}^{\mathrm{BR}}$ and $\boldsymbol{\theta}^{\mathrm{BR}}$ are the angle of departure (AoD) and the angle of arrival (AoA). On the other hand, both $\mathbf{r}^{\mathrm{BR}}$ and $\mathbf{d}^{\mathrm{BR}}$ represents the distances between the (RIS and scatterers) and (BS and scatterers), respectively. We can use the Fresnel approximation to model the spherical wavefront in the near-field model as

$$a_{b,l}(\theta_l^{\mathrm{BR}}, d_l^{\mathrm{BR}}) = \exp\left(j\left[b\,\omega_l^{\mathrm{BR}} + b^2\,\gamma_l^{\mathrm{BR}}\right]\right), \tag{4}$$

where $\omega_l^{\mathrm{BR}} \triangleq f(\theta_l^{\mathrm{BR}})$ and $\gamma_l^{\mathrm{BR}} \triangleq g(\theta_l^{\mathrm{BR}}, d_l^{\mathrm{BR}})$ with

$$f(\phi) = -\frac{2\pi\delta}{\lambda}\sin(\phi), \quad g(\phi, r) = \frac{\pi\delta^2}{\lambda\, r}\cos^2(\phi), \tag{5}$$

where λ is the wavelength as $\lambda = c/f_c$, f_c is the carrier frequency and c is the speed of light, δ is a fixed distance between each of adjacent elements in the ULA. We assume that the reference antenna element to be at the center such that the distance from the reference at the center to the element of index b is $\delta\, b$ where $b \in \mathcal{B}$ and $B \triangleq (N^{\mathrm{B}} - 1)/2$.[2] The vector $\mathrm{diag}\left(\boldsymbol{\rho}^{\mathrm{BR}}\right) \in \mathbb{C}^{L^{\mathrm{BR}} \times L^{\mathrm{BR}}}$ represents the propagation gains between the RIS and BS which can be expressed as

$$\rho_l^{\mathrm{BR}} = \left(\frac{c}{4\pi(r_l^{\mathrm{BR}} + d_l^{\mathrm{BR}})f_c}\right)^{\frac{\mu}{2}} \mathcal{F}, \tag{6}$$

where $\mathcal{F}$ is a random variable representing the fading to account for NLoS propagation with and without the RIS and modeled as a standard complex Gaussian, μ is the path loss exponent. The channel model between the UE and the RIS $\mathbf{H}^{\mathrm{UR}}$ is modeled in a similar way. The channel model in (2) considers all paths to pass through the RIS, while the other NLoS propagation are compensated using the probabilistic gain model in (6).

III. Sensing and Localization Based on LiDAR-assisted RIS Network

The goal is to estimate the UE location using a LiDAR-assisted RIS network. The proposed solution includes two phases: (1) We utilize Webots: an open-source computer 3D robot simulator to simulate a scenario of interest and extract LiDAR data. The LiDAR data is processed to extract the scatterers' locations which will be fed to the CS algorithm as partial support. (2) The CS-based localization algorithm will take the partial support in addition to the received signal as an input and extract the UE location as an output. Fig. 2 shows a screenshot of the utilized simulated scenario.

A. Data Processing

In the following, we describe the proposed LiDAR data processing steps:

[1]The received power is proportional to the square of the number of RIS elements [10].

[2]Without loss of generality, we assume N^{B} to be an odd number.

1) Data filtering: the first step is to remove any unwanted data outside the desired region of interest (ROI). In our scenario, the data that represent the ground, as well as the data that represents the building, will be removed using a modified simple morphological filter (SMRF) and density-based spatial clustering of applications with noise (DBSCAN) algorithms [12], [13], respectively. The ground data is considered as an unwanted noise while the building data is an unwanted disturbance that blocks the LoS signals.[3]

2) Downsampling:: We select η random points uniformly to reduce the number of measured points to η, thereby minimizing the computational efforts required for processing the LiDAR data.

3) DBSCAN clustering: we identify the scatterers in the environment by dividing the points cloud into multiple clusters, each representing a scatterer. The DBSCAN has been chosen as a clustering technique due to the fact that DBSCAN doesn't require the number of clusters. The DBSCAN labels the clusters by measuring the portions in the cloud with high spatial density given the shortest distance between the points ϵ and the minimum number of points per cluster $N^{\min}$.

4) scatterers localization: the final step is to extract the scatterers' locations as a set of distances and angles $\mathcal{T}$. For each identified scatterer, the centroid of the scatterer is firstly calculated by measuring the geometric mean along the portion of data that belongs to each scatterer

$$x_l^C = \frac{\sum \tilde{\mathbf{x}}_l}{N_l}, \;\; y_l^C = \frac{\sum \tilde{\mathbf{y}}_l}{N_l}, \;\; z_l^C = \frac{\sum \tilde{\mathbf{z}}_l}{N_l}, \tag{7}$$

where x_l^C, y_l^C, and z_l^C is the centroid of the l-th scatterer with number of points N_l. By calculating the distances between these centroids and the BS, and the RIS known locations, it is possible to recover a subset of scatterers locations $\mathcal{T}$.

B. Compressive Sensing With Partial Support

The standard CS may suffer from errors due to insufficient measurements. The set of the recovered scatterers locations $\mathcal{T}$ will be used to enhance the CS accuracy. Similar to [6], the goal is to estimate the UE location by recovering the AoAs, AoDs, and their co-responding distances from the received signal. However, applying the CS directly on the received signal in (1) is a complex task as the utilized near-field model in (4) requires the construction of a two dimensional (2D) dictionary matrix over all possible angles and distances [11]. To solve this problem, we consider exploiting the spatial correlation in the channel model, more specifically, consider multiplying the steering response in (4) with its conjugate

$$\begin{aligned} &a_{b,l}(\phi_l^{\mathrm{BR}}, r_l^{\mathrm{BR}}) a_{k,p}(\phi_k^{\mathrm{BR}}, r_k^{\mathrm{BR}})^* \\ &= \exp\left(j\,[b\,\omega_l^{\mathrm{BR}} + b^2\,\gamma_l^{\mathrm{BR}}]\right) \exp\left(j\,[p\,\omega_k^{\mathrm{BR}} + p^2\,\gamma_k^{\mathrm{BR}}]\right)^* \\ &= \exp\left(j\,b\,\omega_l^{\mathrm{BR}} + jb^2\,\gamma_l^{\mathrm{BR}} - j\,p\,\omega_k^{\mathrm{BR}} - jp^2\,\gamma_k^{\mathrm{BR}}\right). \end{aligned} \tag{8}$$

For selected antenna elements $p = -b$ with the same propagation path $l = k$, (8) can be simplified to

$$a_{l,b}(\phi_l^{\mathrm{BR}}, r_l^{\mathrm{BR}}) a_{l,-b}(\phi_k^{\mathrm{BR}}, r_k^{\mathrm{BR}})^* = \exp\left(2j\,b\,\omega_l^{\mathrm{BR}}\right). \tag{9}$$

[3]We consider the building and ground in the NLoS propagation; however, without loss of generality, it might be considered as a non-given support.

Using this methodology, we removed the term $b^2\,\gamma_l^{\mathrm{BR}}$ from (4) which is a function of two variables, i.e., $\gamma_l^{\mathrm{BR}} \triangleq g(\theta_l^{\mathrm{BR}}, d_l^{\mathrm{BR}})$. The remaining term $2j\,b\,\omega_l^{\mathrm{BR}}$ in (9) is a function of only one variable, i.e., $\omega_l^{\mathrm{BR}} \triangleq f(\theta_l^{\mathrm{BR}})$. We generalize this idea by constructing $\mathbf{V}$ that includes properly selected elements of the covariance matrix of the actual channel, such that the $v_{b,u}$ element can be represented as

$$v_{b,u} \triangleq \mathbb{E}\{h_{b,u} {h_{p,n}}^*\}, \forall u \in \mathcal{U}, b \in \mathcal{B}, p = -b, n = -u. \tag{10}$$

The matrix $\mathbf{V}$ can be estimated using T snapshots as

$$\tilde{v}_{b,u} = T^{-1} \sum_{t=1}^{T} \hat{h}_{b,u}[t] \hat{h}^*_{-b,-u}[t] + \nu, \forall\, u \in \mathcal{U}, b \in \mathcal{B}, \tag{11}$$

where $\hat{h}_{b,u}$ correspond to the least square (LS) estimation of the channel, i.e., $\hat{\mathbf{H}} = \mathbf{Y}\mathbf{X}^{\dagger}$, while ν corresponds to the errors due to the limited number of snapshots, imperfect LS channel estimation, and the noise on the received signal. We can reformulate (11) as

$$\tilde{\mathbf{V}} = \;\; \mathbf{S}^1(\boldsymbol{\phi}^{\mathrm{BR}})\mathbf{C}^1 + \boldsymbol{\Upsilon}, \tag{12}$$

where $\mathbf{C}^1 \in \;\mathbb{C}^{L^{\mathrm{BR}} \times M}$ is the support matrix, $\boldsymbol{\Upsilon}$ accounts for the errors, and $\mathbf{S}^1(\boldsymbol{\phi}^{\mathrm{BR}}) \in \;\mathbb{C}^{B \times L^{\mathrm{BR}}}$ is defined as

$$\mathbf{S}^1(\boldsymbol{\phi}^{\mathrm{BR}}) = \left[e^{2jb\omega(\phi_1^{\mathrm{BR}})}, e^{2jb\omega(\phi_2)^{\mathrm{BR}}}, \ldots, e^{2jb\omega(\phi_{L^{\mathrm{BR}}}^{\mathrm{BR}})}\right]. \tag{13}$$

In order to solve the above problem using CS, we re-represent (12) by exploiting the spatial sparsity in the angles as

$$\tilde{\mathbf{V}} = \;\; \bar{\mathbf{S}}^1(\boldsymbol{\phi}^{\mathrm{BR}})\bar{\mathbf{C}}^1 + \boldsymbol{\Upsilon}, \tag{14}$$

where $\bar{\mathbf{S}}^1(\boldsymbol{\phi}^{\mathrm{BR}}) \in \;\mathbb{C}^{B \times N}$ is the dictionary matrix such that its n-th column $\bar{\mathbf{s}}_n^1(\boldsymbol{\phi}^{\mathrm{BR}})$ corresponds to the specific angle $(2\pi n - \pi(N+1))/(N-1)$ in the grid of N possible angles.

The problem in (14) can be solved using conventional CS sparse recovery techniques [14]; however, such techniques do not account for the partial known support. The knowledge of the known support can be exploited as in [15]; however, this work is limited to single measurement vector (SMV) models. A more general multiple measurement vector (MMV)-based CS is proposed in [16] where (14) can be re-formulated as

$$\begin{aligned} \underset{\bar{\mathbf{C}}^1}{\text{minimize}} \quad & \sum_{n}^{N} w_n \, ||\bar{\mathbf{c}}_{n*}^1||_{2,1} \\ \text{subject to} \quad & ||\bar{\mathbf{S}}^1(\boldsymbol{\phi}^{\mathrm{BR}})\bar{\mathbf{C}}^1 - \tilde{\mathbf{V}}||_F \leq \kappa, \end{aligned} \tag{15}$$

where κ is a threshold that is related to the noise variance, and w_n represents a given weight over all the possible columns of $\bar{\mathbf{C}}^1$ such that

$$w_n = \begin{cases} 0 & \text{if } n \in \mathcal{T}, \\ 1 & \text{if } n \notin \mathcal{T}. \end{cases} \tag{16}$$

After solving (15), it is possible to extract the recovered angles $\hat{\boldsymbol{\phi}}^{\mathrm{BR}}$ by locating the index of the non-zero rows of $\hat{\mathbf{C}}^1$.

To estimate the distances $\mathbf{r}^{\mathrm{BR}}$ that correspond to the estimated angles $\hat{\boldsymbol{\phi}}^{\mathrm{BR}}$, we substitute in the received signal model (1) which can be re-written as

$$\mathbf{Y} = \mathbf{A}(\hat{\boldsymbol{\phi}}^{\mathrm{BR}}, \mathbf{r}^{\mathrm{BR}})\mathbf{C}^2 + \mathbf{Z}, \tag{17}$$

This article has been accepted for publication in IEEE Wireless Communications Letters. This is the author's version which has not been fully edited and content may change prior to final publication. Citation information: DOI 10.1109/LWC.2023.3311730

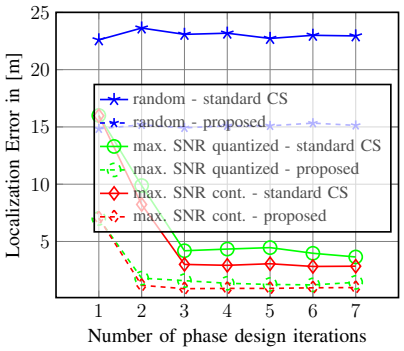

Fig. 3: Localization error versus the numbers of phase design iterations.

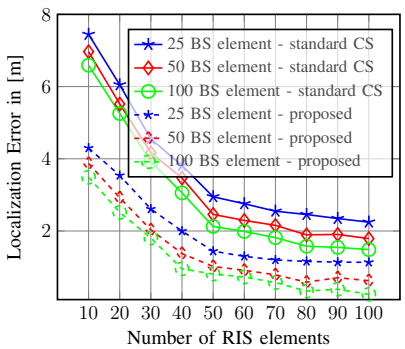

Fig. 4: Localization error versus the number of RIS elements.

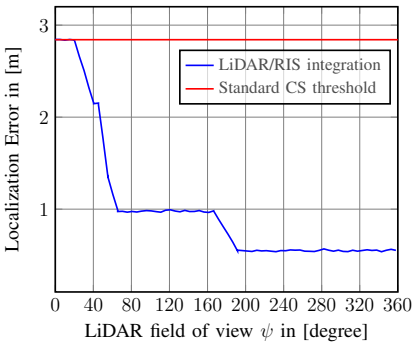

Fig. 5: LiDAR field of view versus localization error.

TABLE I: The simulation parameters.

Description	Parameter	Value
frequency	f_c	28 GHz
Number of antennas (elements)	$N^{\mathrm{B}}/N^{\mathrm{U}}/N^{\mathrm{R}}$	51/21/100
path loss exponent	μ	3
Number of PRSs streams	M^{o}	60
BS location	$\mathbf{p}^{\mathrm{B}}$	[0 0]
RIS location	$\mathbf{p}^{\mathrm{R}}$	[5 5]
UE location	$\mathbf{p}^{\mathrm{U}}$	[15 0]
Bandwidth	B_t	10 MHz
Power	P	1 Watt
LiDAR horizontal field of view	ψ	15°
LiDAR number of layers	N^{layers}	64
Number of Downsampling points	η	1500
Number of scatterers	$L^{\mathrm{BR}}/L^{\mathrm{UE}}$	4/4

where $\mathbf{C}^2$ is the support matrix. We use the methodology in (14) and (15) to recover $\hat{\mathbf{r}}^{\mathrm{BR}}$. We can estimate the other parameters in the RIS-UE side of the channel by computing the Hermitian transpose of $\tilde{\mathbf{V}}^H$ and $\mathbf{Y}^H$ in (14) and (17).

Finally, we utilize the off-grid estimation and the RIS phase design proposed in [6]. The RISs design begins with a random phase and iteratively refines the location estimate. After each iteration, the RIS is re-adjusted until error saturation. Simultaneously, we account for the off-grid errors by minimizing the squared Frobenius norm of the difference between the estimated covariance matrix and the bias mismatch error caused by off-grid discrepancies.

IV. NUMERICAL RESULTS

In order to analyze the performance of our scheme, we propose using computer-programmed 3D simulators to create virtual LiDAR 3D cloud data. This approach addresses limitations in generating actual 3D cloud data for LiDARs, such as cost, effort, time consumption, and complexity. Utilizing actual data remains possible and may be considered in different contexts or future works. Within these constraints, we used Webots [17], a computer-programmed 3D simulator, to model a realistic localization scenario, see Fig. 2. Other works in literature have shown that simulator-based LiDAR virtual data can maintain high validity. For instance, [18] used a computer 3D simulator (e.g., Unreal Engine 4) to generate a scenario and data of LiDAR working against weather conditions. As shown in Fig.2, the user is in a city environment with multiple static and dynamic scatterers such as trees, street lamps and signs, and movable vehicles. A building blocks the direct LoS between the BS and the UE. The white lines in Fig. 2 correspond to the LiDAR horizontal field of view. The LiDAR scans the street portion of our scenario, and some scatterers can be scanned by the LiDAR while others are outside its field of view. The LiDAR scans the environment in the simulation and extracts measurements as 3D cloud data, represented by the vectors $\hat{\mathbf{x}}$, $\hat{\mathbf{y}}$, and $\hat{\mathbf{z}}$, which will be the input of our proposed LiDAR data processor.

Table I presents the simulation parameters. We utilized MATLAB to simulate the channel model and to conduct all the processing. The noise as a thermal noise such that $\sigma_z^2 = B_t\, T_{\mathrm{k}}\, K$ where B_t represents the bandwidth, K is Boltzmann constant, and $T_{\mathrm{k}} = 290$ is the room temperature measured in Kelvin. We consider the JointBP YALL1 group solver [16] to solve the CS problems. The simulations are conducted using Monte Carlo technique with 10000 iterations.

In Fig. 3, we compute the localization error against the number of phase design iterations for different RIS phase design schemes: random, max. SNR cont., max. SNR quantized. We simulated the proposed LiDAR-assisted RIS network against the standard CS. The results reveal a 65% reduction in localization error using SNR maximization phase design. This error reduction is attributed to the given partial support that lessened the recovery error of the CS. Utilizing LiDAR ensures minimal error in estimating the scanned scatterers' location and significant reduction in estimating the non-scanned (non-visible) scatterers. Additionally, minimizing the error of estimating both scanned and non-scanned scatterers improves the RIS phase design. On the other hand, the proposed scheme needs two iterations of RIS phase design to saturate, while the standard CS takes three on average.

In Fig. 4, we compare the localization performance of the proposed LiDAR-assisted RIS network against the standard CS for different simulation parameters. We vary the number of RIS elements N^{R} from 0 to 100 and repeat the simulation for different numbers of BS elements N^{B}. The results show the superior performance of the proposed LiDAR-assisted RIS network in comparison to the standard CS. The figure shows that we can achieve better performance using an RIS with a large number of elements.

In Fig. 5, we investigate the effect of the LiDAR horizontal field of view angle ψ on the localization error. With a higher field of view, the LiDAR will be able to detect more scatterers' locations, achieving higher localization accuracy. We used the same number of downsampling points η over all the field of view angles. In other words, when ψ is small, all the η points

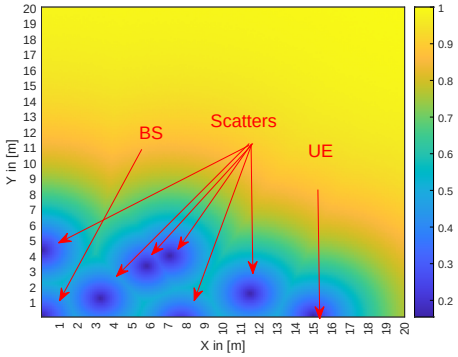

Fig. 6: Localization error for different RIS locations.

TABLE II: Computational time.

Number of RIS elements N^{R}	Number of BS elements N^{B}	Algorithm	
		proposed	standard CS
		Time in [s]	
64	51	1.1285	2.0003
	75	6.15195	10.9214
128	51	1.4341	2.5154
	75	6.6874	11.7765

will be distributed on a small number of objects, while with wider ψ, the η points will be more sparse per object due to the distribution over multiple objects. This fact has been reflected in the curve as a flatter slope of error with objects of higher angles. The curve also shows that with very small ψ (i.e., the LiDAR didn't detect any scatterer), the localization error is almost similar to the case of the standard CS with no LiDAR in Fig. 3.

We validate the effect of the geometrical layout on the localization error using Fig. 6 which represents a heat map of the localization error as a function of the RIS location in the XY-plane. the figure shows that the localization error can be decreased when we place the RIS in the proximity of the scatters, BS, or the UE. More specifically, the results show that the localization error decreases to less than 0.2(m) when we place the RIS 1(m) away from the wireless system elements. The achieved results are expected as placing the RIS near the scatterer can improve the performance by enhancing the signal strength or adjusting the signal's direction of arrival.

In Table II, we computed the required simulation time to localize the UE using both the proposed LiDAR-assisted RIS network and the standard CS utilizing a workstation with specifications as shown in Table III. The table shows a significant improvement using the proposed LiDAR-assisted RIS network.

V. CONCLUSION

In this paper, we proposed RIS localization using partial compressed sensing support assisted with LiDAR sensors. The LiDAR scans the environment to estimate the location of the scatterers and fed these locations as partial support to CS-based positioning algorithm. The numerical results show that utilizing such a scheme can minimize the localization error by 65% compared to standard CS, utilizing an RIS of 100 elements. These results can be used to extend this work in the future to address the localization problem with dynamic movable scatterers.

TABLE III: Workstation specifications.

Aspect	Specification
CPU	Intel(R) Core(TM) i5-10500 CPU @ 3.10GHz 3.10 GHz
GPU	Intel(R) UHD Graphics 360
Memory	16.0 GB DDR4-SDRAM
OS	Windows 10 Education 64-bit

REFERENCES

[1] J. Hu, H. Zhang, K. Bian, Z. Han, H. V. Poor, and L. Song, "Metasketch: Wireless semantic segmentation by reconfigurable intelligent surfaces," *IEEE Trans. Wirel. Commun.*, vol. 21, no. 8, pp. 5916–5929, Jan. 2022.

[2] O. Rinchi, A. Elzanaty, and A. Alsharoa, *Wireless Localization with Reconfigurable Intelligent Surfaces*, F. Tariq, M. Khandaker, and I. S. Ansari, Eds. CRC Press, May 2023.

[3] ——, "Single-snapshot localization for near-field RIS model using atomic norm minimization," in *Proc. of the IEEE Conference on Global Telecommunications (GLOBECOM)*, Rio de Janeiro, Brazil, Dec. 2022.

[4] J. He, A. Fakhreddine, H. Wymeersch, and G. C. Alexandropoulos, "Compressed-sensing-based 3D localization with distributed passive reconfigurable intelligent surfaces," in *Proc. of the IEEE International Conference on Acoustics, Speech and Signal Processing (ICASSP)*, Rhodes Island, Greece, June 2023, pp. 1–5.

[5] S. Palmucci, A. Guerra, A. Abrardo, and D. Dardari, "Two-timescale joint precoding design and RIS optimization for user tracking in near-field MIMO systems," *IEEE Trans. Signal Process.*, pp. 1–16, 2023.

[6] O. Rinchi, A. Elzanaty, and M.-S. Alouini, "Compressive near-field localization for multipath RIS-aided environments," *IEEE Commun. Lett.*, vol. 26, no. 6, pp. 1268–1272, Feb. 2022.

[7] S. Wu, C. Chakrabarti, and A. Alkhateeb, "LiDAR-aided mobile blockage prediction in real-world millimeter wave systems," in *Proc. of the IEEE Wireless Communications and Networking Conference (WCNC)*, Austin, TX, USA, May 2022, pp. 2631–2636.

[8] S. Jiang, G. Charan, and A. Alkhateeb, "LiDAR aided future beam prediction in real-world millimeter wave V2I communications," *IEEE Wirel. Commun. Lett.*, vol. 12, no. 2, pp. 212–216, Feb. 2023.

[9] O. Rinchi, A. Alsharoa, and I. Shatnaw, "Deep-learning-based accurate beamforming prediction using LiDAR-assisted network," in *Proc. of the IEEE International Symposium on Personal, Indoor and Mobile Radio Communications (PIMRC)*, Toronto, ON, Canada, Sept. 2023.

[10] Ö. Özdogan, E. Björnson, and E. G. Larsson, "Intelligent reflecting surfaces: Physics, propagation, and pathloss modeling," *IEEE Wirel. Commun. Lett.*, vol. 9, no. 5, pp. 581–585, May 2020.

[11] J. He, H. Wymeersch, and M. Juntti, "Channel estimation for RIS-aided mmwave MIMO systems via atomic norm minimization," *IEEE Trans. Wirel.*, vol. 20, no. 9, pp. 5786–5797, Apr. 2021.

[12] T. J. Pingel, K. C. Clarke, and W. A. McBride, "An improved simple morphological filter for the terrain classification of airborne LIDAR data," *ISPRS J. Photogramm. Remote Sens.*, vol. 77, pp. 21–30, Mar. 2013.

[13] K. Khan, S. U. Rehman, K. Aziz, S. Fong, and S. Sarasvady, "DBSCAN: Past, present and future," in *Proc. of the international conference on the applications of digital information and web technologies (ICADIWT)*. Bangalore, India: IEEE, May 2014, pp. 232–238.

[14] A. Elzanaty, A. Giorgetti, and M. Chiani, "Weak RIC analysis of finite Gaussian matrices for joint sparse recovery," *IEEE Signal Process. Lett.*, vol. 24, no. 10, pp. 1473–1477, July 2017.

[15] N. Vaswani and W. Lu, "Modified-CS: Modifying compressive sensing for problems with partially known support," *IEEE Trans. Signal Process.*, vol. 58, no. 9, pp. 4595–4607, May 2010.

[16] W. Deng, W. Yin, and Y. Zhang, "Group sparse optimization by alternating direction method," in *Wavelets and Sparsity XV*, vol. 8858. SPIE, Sept. 2013, pp. 242–256.

[17] O. Michel, "Cyberbotics ltd. webots™: professional mobile robot simulation," *Int. J. Adv. Robot. Syst.*, vol. 1, no. 1, p. 5, 2004.

[18] J. P. Espineira, J. Robinson, J. Groenewald, P. H. Chan, and V. Donzella, "Realistic LiDAR with noise model for real-time testing of automated vehicles in a virtual environment," *IEEE Sens. J.*, vol. 21, no. 8, pp. 9919–9926, Feb. 2021.